



TSI-GAN: Unsupervised Time Series Anomaly Detection using Convolutional Cycle-Consistent Generative Adversarial Networks

Shyam Sundar Saravanan¹, Tie Luo¹  , and Mao Van Ngo²

¹ Missouri University of Science and Technology, Rolla, MO 65401, USA

² Singapore University of Technology and Design, Singapore 487372
{ssdmw, tluo}@mst.edu, vanmao_ngo@sutd.edu.sg

Abstract. Anomaly detection is widely used in network intrusion detection, autonomous driving, medical diagnosis, credit card frauds, etc. However, several key challenges remain open, such as lack of ground truth labels, presence of complex temporal patterns, and generalizing over different datasets. This paper proposes TSI-GAN, an unsupervised anomaly detection model for time-series that can learn complex temporal patterns automatically and generalize well, i.e., no need for choosing dataset-specific parameters, making statistical assumptions about underlying data, or changing model architectures. To achieve these goals, we convert each input time-series into a sequence of 2D images using two encoding techniques with the intent of capturing temporal patterns and various types of deviance. Moreover, we design a reconstructive GAN that uses convolutional layers in an encoder-decoder network and employs *cycle-consistency loss* during training to ensure that inverse mappings are accurate as well. In addition, we also instrument a *Hodrick-Prescott filter* in post-processing to mitigate false positives. We evaluate TSI-GAN using 250 well-curated and harder-than-usual datasets and compare with 8 state-of-the-art baseline methods. The results demonstrate the superiority of TSI-GAN to all the baselines, offering an overall performance improvement of 13% and 31% over the second-best performer MERLIN and the third-best performer LSTM-AE, respectively.

Keywords: Anomaly detection · time series · unsupervised learning · generative adversarial networks.

1 Introduction

Anomaly detection aims to identify sub-sequences of various lengths that are considered abnormal within a context represented by data. Accurate and automated anomaly detection is crucial to a wide range of applications including network security, smart manufacturing, autonomous driving, and digital healthcare. Time-series data is ubiquitous in almost all application domains; hence, time-series anomaly detection has been actively studied for years, especially recently using machine learning. However, it remains a very challenging task for three key reasons: (i) labels for abnormal data are often rare, preventing proper training of supervised learning models; (ii) real-world time-series data is often subject to noise and characterized by complex temporal patterns that are difficult to identify; (iii) different datasets have different properties and thus often require a specific choice of parameters (e.g., using domain knowledge) for anomaly detectors to work well, making them hard to generalize.

To address these challenges, we propose a novel generative adversarial network (GAN) architecture called TSI-GAN for *unsupervised* time series anomaly detection. First, we encode the input time series to images to capture the temporal correlation and various types of deviance present in the time series, which explains part of our approach, TSI, which stands for *Time Series to Images*. This encoding also allows us to leverage GAN's outstanding performance on tasks of image generation [6] and image-to-image translation [9]. Second, we design a GAN with two critics and two generators that consist of convolutional layers in order to reconstruct the encoded images and obtain effective reconstruction errors. The purpose of the GAN is to learn a generalized distribution of

normal samples such that it produces reconstruction errors that are (i) large on anomalous inputs and (ii) small on normal data even in the presence of noise and time non-stationarity. We also take a fully nonparametric approach throughout our design pipeline and as a result our model does not make any assumptions about the underlying data and does not require choosing parameters for each dataset, or altering model architectures like [25].

In addition, GAN-based methods typically sample a random latent and optimize it using gradient descent as a separate step during *inference* to find the latent representation that would yield an accurate inverse mapping for *each sample* [18,11]. This is highly inefficient on large datasets and impractical for real-time applications as proven by [25]. In contrast, we train an encoder-decoder network in our GAN with *cycle consistency loss* to obtain the latent representation of the inverse mapping automatically and immediately, making our inference almost instantaneous.

Third, as a further enhancement we address false positives (alarms), which are often a pain point in existing anomaly detection methods. To this end, we post-process the reconstruction errors using the *Hodrick-Prescott filter* [7] and then combine the errors from two encoding channels using a weighted sum. This way, we obtain a reliable anomaly score vector which leads to reduced false positives.

In summary, this paper makes the following contributions:

- We introduce TSI-GAN, a novel convolutional cycle-consistent GAN architecture that learns to reconstruct 2D-encoded complex 1D time-series data and produces reliable reconstruction errors for detecting non-trivial time series anomalies without any labels, and in real-time.
- We address the challenge of model generalization by taking a fully nonparametric approach throughout our design pipeline. As a result, our method makes no assumptions about underlying data and requires no manual parameter choice, or changing model architectures.
- We mitigate false alarms as a common issue in anomaly detection, by post-processing the reconstruction error using a filtering technique and a weighting strategy.
- We benchmark TSI-GAN against eight state-of-the-art baseline methods on 250 well-curated and harder-than-usual datasets. The results validate our approach as the best performer overall, with a large winning margin over other methods.

Our results are fully reproducible, with code open-sourced at <https://github.com/LabSAINT/TSI-GAN>.

2 Related work

Due to the importance of anomaly detection in many applications, research in this field has been active for years. While statistical methods are traditionally applied, machine learning and especially deep learning-based approaches have recently received increasingly more attention due to their attractive performance. These methods can generally be classified into:

Proximity-based methods classify a data point as a point anomaly or a subsequence as a collective anomaly when its locality is sparsely populated. These methods can be further classified into *cluster-based methods* such as k-means clustering [3], *distance-based methods* such as k-nearest neighbors [1], and *density-based methods* such as DBSCAN [2]. The main drawback of these methods when applied to time series anomaly

detection is that they require the number of anomalies to be known a priori and are unable to capture temporal patterns. Time-series discord discovery [24] is a recently proposed distance-based method that identifies very unusual subsequences in a time series. Under this category, Nakamura et al. introduced MERLIN [13], which is considered to be the state-of-the-art for anomaly detection in univariate time series and is included as a baseline in our experiments.

Prediction-based methods try to predict future values of a time series and classify a data point as an anomaly if the predicted value differs from the real data by more than a specified threshold. Time series forecasting methods such as ARIMA [15] can be used, but they often require extensive examination and preprocessing of data and are sensitive to parameters. Several deep-learning approaches have been proposed to overcome these limitations. For example, Hundman et al. [8] proposed an LSTM model with dynamic thresholding (LSTM-DT) to make predictions and reduce false positives.

Reconstruction-based methods learn a latent low-dimensional representation of the input time-series data and try to reconstruct the input based on the representation. The assumption is that anomalies will lose information when mapped to the latent space and thus will not be reconstructed accurately, producing a larger reconstruction error. Hence, reconstruction error is measured at each time step and thresholding techniques are applied to detect the anomalies. Several deep learning approaches have been proposed including LSTM-based Autoencoder (LSTM-AE) [14], Dense Autoencoder (DENSE-AE) [17], DONUT [22] which uses a Variational Autoencoder (VAE), and GAN-based methods [5,18,11]. TadGAN [5] presents a recent study using GAN to perform this task and it is considered to be state-of-the-art in terms of GAN-based methods.

However, TadGAN uses 1-D representation and requires the sampling interval of input data to be known for data preprocessing; otherwise, anomalies that do not have extreme amplitude (either high or low relative to other points) will not be detected. This is a notable limitation because most anomalies in the real world are complicated rather than just simple amplitude spikes or dips. Another related work is T2IVAE [23], which transforms time series to images and uses VAE to reconstruct the input time series. However, VAEs are prone to overfitting and often reconstruct anomalous samples quite accurately, resulting in unreliable reconstruction errors. Even though T2IVAE attempts to reduce this risk by employing an adversarial training strategy in the last five training epochs, the overfitting effect remains rather prominent.

We take a GAN-based approach instead of VAE because we find that GAN is strongly averse to the overfitting phenomenon when it comes to infrequent anomalous samples and unlike TadGAN we 2D encode the input time series and use CNN layers in our GAN to learn feature maps as if learning from images. This way, we are able to encode temporal information/correlation and capture various types of deviance and thus obtain more accurate and reliable anomaly scores based on reconstruction errors.

There are also **commercial tools** including Microsoft Azure Anomaly Detector [16] and LinkedIn Luminol [12]. Azure uses spectral residual (SR) from the saliency detection domain [16] and CNN to learn a discriminating threshold. The output is a sequence of labels indicating if a particular timestamp is anomalous. Luminol uses the Bitmap detector algorithm [20] which divides input time series into chunks and calculates the frequency of similar chunks to calculate anomaly scores. These commercial tools are included as baselines in our experiments as well.

3 Encoding Time-series to Images

The core idea behind encoding the time-series to images is that if any time step is anomalous, then the row and column corresponding to that time step in the encoded image will be significantly different from other normal pixels (see Fig. 1) and thus could be easily detected by a reconstruction-based model. Consider an input time series $\mathring{X} = \{x_1, x_2, \dots, x_T\}$, where T is the time series length. We use a sliding window with window size W and step size S to divide \mathring{X} into N overlapping sub-sequences, $\mathring{X}_k = \{x_{k+1}, x_{k+2}, \dots, x_{k+W}\}$, where $k = 0, \dots, N-1$ and $N = \lfloor \frac{T-W}{S} \rfloor$. We set $W = 64$ and $S = 1$ and convert each window of size 64 into a two-channel image of size $64 \times 64 \times 2$, using two time-series encoding techniques: Gramian Angular Field (GAF) [19] and Recurrence Plot (RP) [4].

3.1 Gramian Angular Field (GAF)

Given a sub-sequence $\mathring{X}_k = \{x_{k+i}\}_{i=1}^W$ at time step k , GAF rescales all the observations into the interval $[-1, 1]$ and calculates $\bar{X}_k = \{\bar{x}_{k+i}\}_{i=1}^W$, where

$$\bar{x}_{k+i} = \frac{(x_{k+i} - \max(\mathring{X}_k)) + (x_{k+i} - \min(\mathring{X}_k))}{\max(\mathring{X}_k) - \min(\mathring{X}_k)}$$

Next, we represent each rescaled \bar{X}_k using polar coordinates, as radius $r = t_{k+i}/W$ where $t_{k+i} \in \mathbb{N}$ is the timestamp, and angular $\phi = \arccos(\bar{x}_{k+i}) \in [0, \pi]$. This polar conversion produces a one-to-one mapping with a unique inverse function and preserves absolute temporal relation (as opposed to Cartesian coordinates). Thus, we can identify the temporal correlation at different time intervals by calculating the trigonometric sum between each point within the sub-sequence:

$$X_k^{GAF} = (\bar{X}_k)^T \otimes \bar{X}_k - \left(\sqrt{I - (\bar{X}_k)^2} \right)^T \otimes \sqrt{I - (\bar{X}_k)^2}$$

where X_k^{GAF} is a $W \times W$ matrix, I is the unit row vector $[1, 1, \dots, 1]$ (\bar{X}_k is a row vector too), and \otimes represents outer product.

3.2 Recurrence Plot (RP)

A recurrence plot (RP) [4] is an image that represents the distance between observations extracted from a sub-sequence time series. Given a sub-sequence window $\mathring{X}_k = \{x_{k+i}\}_{i=1}^W$, we calculate a RP matrix X_k^{RP} of dimension $W \times W$ where each element at row a and column b is defined as

$$x_{k,(a,b)}^{RP} = \Theta(\epsilon - \|x_{k+a} - x_{k+b}\|), \forall a, b \in \{1, \dots, W\} \quad (1)$$

where $\Theta(\cdot) : \mathbb{R} \rightarrow \{0, 1\}$ is a Heaviside function, and ϵ is a predefined distance threshold. In this work, instead of using binary representation, we use raw distances $\|x_{k+a} - x_{k+b}\|$ (without the need for choosing ϵ or $\Theta(\cdot)$) to construct the RP matrix; the resulting 2D image will thus have more granularity scales of the distances. In order to align RP images with GAF images on the same scale, we scale the RP matrix into the range $[-1, 1]$ before further processing.

3.3 Combining two channels

After encoding the series using GAF and RP, respectively, we treat them as two channels and stack them along the channel axis to obtain:

$$X_k = \text{Stack}(X_k^{GAF}, X_k^{RP})$$

Since we have divided the original time series \mathring{X} into N overlapping sub-sequence windows of size W , and encoded each window as a 2-channel image of shape $[W \times W \times 2]$, we thus finally obtain a sequence of images $\mathbb{X} = \{X_k\}_{k=1}^N$.

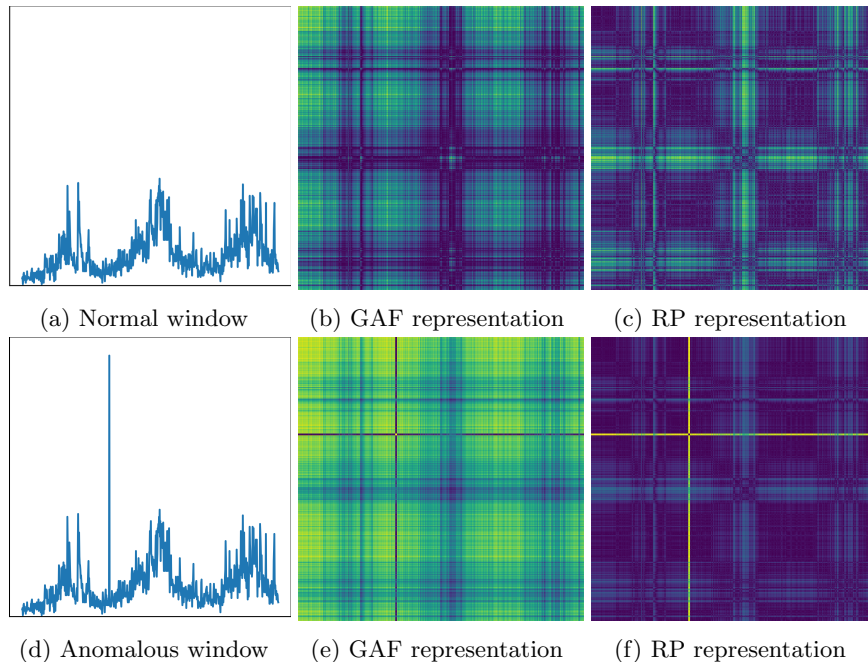


Fig. 1: Illustration of normal (top row) and anomalous (bottom row) windows encoded by GAF and RP, for an example time-series.

4 The TSI-GAN Model

4.1 Model Architecture

Reconstruction-based anomaly detection methods learn a model that maps input data (in our case, an image with two channels) to the latent low-dimensional space and then reconstructs the input using the latent representation. The objective is to train a model that captures a generalized latent representation of the *normal* patterns, such that anomalies will *not* be reconstructed accurately and hence result in a larger reconstruction error. In our proposed method, we learn two mapping functions, $\mathcal{E} : \mathcal{X} \rightarrow \mathcal{Z}$ and $\mathcal{G} : \mathcal{Z} \rightarrow \mathcal{X}$, where \mathcal{X} represents the input domain, \mathcal{Z} represents the latent domain for which Gaussian distribution $\mathcal{N}(0, 1)$ is used. For any given input image at time step k , denoted by X_k , the model tries to reconstruct it as $X_k \rightarrow \mathcal{E}(X_k) \rightarrow \mathcal{G}(\mathcal{E}(X_k)) \approx \hat{X}_k$.

The entire model architecture is presented in Fig. 2. We model the above mapping functions as Generators, where \mathcal{E} acts as an encoder which maps the input image to the latent space using convolution layers, and \mathcal{G} acts as a decoder which transforms the latent representation to a reconstructed input image using transposed convolution. We use two Critics \mathcal{C}_x and \mathcal{C}_z : \mathcal{C}_x regulates the decoder \mathcal{G} by trying to distinguish real images X from the reconstructed images $\mathcal{G}(\mathcal{E}(x))$; \mathcal{C}_z regulates the encoder \mathcal{E} by trying to liken the latent representation $\mathcal{E}(x)$ to the Gaussian noise z . The L_2 -norm will be used in our cycle consistency loss which we describe later in Section 4.2.

4.2 Loss Function and Training Strategy

We use two loss functions: (1) Wasserstein loss, to match the distribution of generated images with the distribution of input images, and (2) cycle consistency loss, to ensure the desired mapping route $X_k \rightarrow Z_k \rightarrow \hat{X}_k$.

Wasserstein Loss: We train the generator \mathcal{G} and its critic C_x with Wasserstein loss:

$$\min_{\mathcal{G}} \max_{C_x \in \mathbf{C}_x} L_X(C_x, \mathcal{G}) \triangleq \mathbb{E}_{x \sim \mathbb{P}_X} [C_x(x)] - \mathbb{E}_{z \sim \mathbb{P}_Z} [C_x(\mathcal{G}(z))] \quad (2)$$

Similarly, for Encoder \mathcal{E} and its Critic C_z , the loss function is defined as:

$$\min_{\mathcal{E}} \max_{C_z \in \mathbf{C}_z} L_Z(C_z, \mathcal{E}) \triangleq \mathbb{E}_{z \sim \mathbb{P}_Z} [C_z(z)] - \mathbb{E}_{x \sim \mathbb{P}_X} [C_z(\mathcal{E}(x))] \quad (3)$$

where \mathbf{C}_x and \mathbf{C}_z are the set of all the 1-Lipschitz functions.

We also add a gradient penalty regularization term to both (2) and (3) to ensure a 1-Lipschitz continuous Critic so that Wasserstein Loss validly approximates the *Earth Mover’s Distance* [10]. The complete architecture is presented in Table 1 and Figure 2.

Cycle Consistency Loss: The GAN model described above is able to map X_k to a desired Z_k . However, the inverse mapping of Z_k back to \hat{X}_k is not guaranteed by training with just Wasserstein losses alone. This is because those losses only ensures distribution similarity but not instance similarity. To this end, Schlegl et al. [18] proposed an iterative approach where they sample a random latent and optimize it using gradient descent as a separate step during *inference* to find the best Z_k that would generate $\mathcal{G}(\mathcal{E}(X_k))$ that is most similar to the input image X_k . However, this method suffers from large search space and is inefficient for large datasets and real-time applications, as shown by Zenati et al. [25]. Hence, we use *cycle-consistency loss* [26] to train the generators \mathcal{E} and \mathcal{G} :

$$\min_{\mathcal{E}} L_{CL}(\mathcal{E}) \triangleq \mathbb{E}_{x \sim \mathbb{P}_X} \|x - \mathcal{G}(\mathcal{E}(x))\|_2 + \mathbb{E}_{z \sim \mathbb{P}_Z} \|z - \mathcal{E}(\mathcal{G}(z))\|_2 \quad (4)$$

For \mathcal{G} we only use the forward consistency loss, as the backward consistency loss (i.e., $\mathbb{E}_{z \sim \mathbb{P}_Z} \|z - \mathcal{E}(\mathcal{G}(z))\|_2$) has been integrated into (4) and thus is not necessary for \mathcal{G} :

$$\min_{\mathcal{G}} L_{CL}(\mathcal{G}) \triangleq \mathbb{E}_{x \sim \mathbb{P}_X} \|x - \mathcal{G}(\mathcal{E}(x))\|_2. \quad (5)$$

Final Objective Combining the objectives (2), (3), (4), (5) we arrive at the final objective:

$$\min_{\{\mathcal{E}, \mathcal{G}\}} \max_{\{C_x \in \mathbf{C}_x, C_z \in \mathbf{C}_z\}} L_X(C_x, \mathcal{G}) + L_Z(C_z, \mathcal{E}) + L_{CL}(\mathcal{E}) + L_{CL}(\mathcal{G}) \quad (6)$$

4.3 Post-processing and Anomaly Detection

Unlike other anomaly detection methods, we added a post-processing procedure to achieve a more reliable detector, as follows. We then extract the reconstruction error for each channel as ϵ_{gaf} and ϵ_{rp} (refer lines 1-5 in Algorithm 1). Calculating thresholds directly on the raw reconstruction error will lead to many false positives. To mitigate this, we smooth the reconstruction error to suppress frequently occurring minor error peaks which are usually caused by normal behavior rather than anomalies. We use the

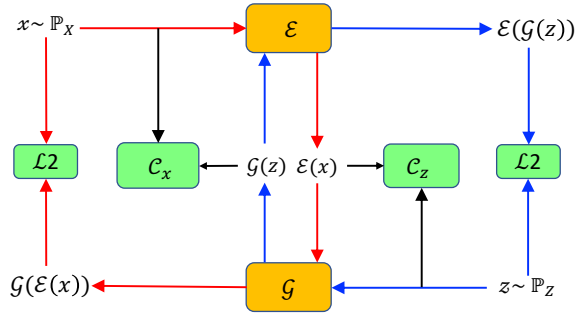


Fig. 2: TSI-GAN model architecture: \mathcal{E} is the encoder and \mathcal{G} the decoder; C_x and C_z are the critics.

Hodrick-Prescott filter [7] because of its excellent capability of removing short-term fluctuations in data since we are only concerned with peaks that persist for a sustained period of time. It extracts a smooth trend r from a given sequence ϵ of length N by solving:

$$\min_r \left(\sum_{k=1}^N (\epsilon_k - r_k)^2 + \lambda \sum_{k=2}^{N-1} [(r_{k+1} - r_k) - (r_k - r_{k-1})]^2 \right)$$

Algorithm 1: Anomaly Detection using TSI-GAN

```

// Compute reconstruction errors
1 for  $k=1, \dots, N$  do
2    $\hat{X}_k \leftarrow \mathcal{G}(\mathcal{E}(X_k))$ 
3    $\hat{X}_k^{GAF}, \hat{X}_k^{RP} \leftarrow$  extract GAF & RP channels
   from  $\hat{X}_k$ 
4    $\epsilon_{gaf_k} \leftarrow \sum_{i=1}^W \sum_{j=1}^W (X_{k,i,j}^{GAF} - \hat{X}_{k,i,j}^{GAF})^2$ 
5    $\epsilon_{rp_k} \leftarrow \sum_{i=1}^W \sum_{j=1}^W (X_{k,i,j}^{RP} - \hat{X}_{k,i,j}^{RP})^2$ 
// Post-processing to obtain anomaly scores
6 for  $ch \in \{gaf, rp\}$  do
7    $\epsilon_{ch} \leftarrow$  HP( $\epsilon_{ch}$ ) // Hodrick-Prescott filter
8    $peaks_{ch} \leftarrow$  find_peaks( $\epsilon_{ch}$ )
9    $\sigma_{ch} \leftarrow \frac{(peaks_{ch}[0] - peaks_{ch}[1])}{peaks_{ch}[0]} + 1$ 
10  $score\_vec \leftarrow \sigma_{gaf} \times \epsilon_{gaf} + \sigma_{rp} \times \epsilon_{rp}$ 
// Detect anomalies
11  $mean \leftarrow$  mean( $score\_vec$ )
12 for  $k=1, \dots, N$  do
13   if  $score\_vec_k > mean$  then
14     |  $pred_k = true$ 
15   else
16     |  $pred_k = false$ 
17 Group consecutive  $pred_k$ 's into  $\{seq_i\}_{i=1}^L$ 
// Pruning to reduce false alarms
18  $\{m_i\} \leftarrow$  max( $\{seq_i\}$ )
19  $\{m_i\} \leftarrow$  sort( $\{m_i\}, descending=true$ )
20 sort  $\{seq_i\}$  in the same order of  $\{m_i\}$ 
21 for  $i=1, \dots, L$  do
22    $p_i \leftarrow (m_{i-1} - m_i) / m_{i-1}$ 
23   if  $p_i < \theta$  then
24     | reclassify  $\{seq_j\}_{j=i}^L$  as normal
25     | break;
```

After smoothing ϵ_{gaf} and ϵ_{rp} , we find the local (neighborhood) peaks in each channel and sort them in descending order to calculate a confidence level $\sigma \in [1, 2]$ for each channel:

$$\sigma = \frac{peaks[0] - peaks[1]}{peaks[0]} + 1,$$

where $peaks[0]$ and $peaks[1]$ are the first and the second highest peaks in the smoothed reconstruction errors, respectively. The idea is that when the difference between these two peaks is large, that channel is assumed to be more confident about its detection of the anomaly and hence weighed higher in the final anomaly score. This score is defined by combining the two reconstruction errors ϵ_{gaf} and ϵ_{rp} using their respective confidence level (see line 10 in Algorithm 1). Here it is defined as a vector (of length N) because each of the N windows will have an anomaly score. For the weight σ , if there are multiple anomalies, the difference between $peaks[0]$ and $peaks[1]$ will be small and thus σ will be smaller than the other channel if the other channel detects a single outlier, which is desired since outliers are rare by defini-

tion and thus single outliers are more likely than multiple. Otherwise, if both channels detect multiple, they will be weighted by similar σ 's.

After obtaining the anomaly score for each window, we calculate the mean anomaly score over all the windows and any window that exceeds this threshold is flagged as an

Property	Dataset						
	AirTemperature	PowerDemand	InternalBleeding	EPG	NASA T-1	Noise	All datasets
# Sub-datasets	14	8	26	12	10	16	250
# Data Points	98208	239448	194992	359304	113488	629494	19353766
# Anomalous Points	398	1688	3018	1292	644	3134	49363
# (% tot.)	0.004%	0.007%	0.015%	0.003%	0.005%	0.004%	0.002%

Table 2: Statistics of Datasets used in our experiments.

anomaly. Following that, consecutive anomalous windows will be grouped together to form a sequence (i.e., collective anomaly). Finally, we use an anomaly pruning approach (lines 17-25 in Algorithm 1) introduced by Hundman et al. [8], to further mitigate false positives. The above post-processing and detection procedures are formulated in Algorithm 1.

5 Performance Evaluation

5.1 Datasets

We use the UCR 2021 anomaly detection dataset³ which contains 250 sub-datasets collected from a variety of sources. Unlike commonly used datasets such as Yahoo, Numenta, and NASA which are found to have numerous flaws [21] including incorrect ground truth labels, triviality of the anomalies, and unrealistic anomaly density, this UCR dataset is carefully curated, harder to detect and is much more reliable. Moreover, this dataset contains a combination of point, collective, and contextual anomalies as well as amplitude, seasonal, and trend anomalies, which offers a good variety for evaluation.

We choose a total of 6 categories from this dataset and each category contains 4-13 original sub-datasets; each original sub-dataset comes with a distorted duplicate by adding artificial fluctuations. Therefore, the number of sub-datasets is doubled. The only exception is the **Noise** category in which the sub-datasets are chosen from multiple other categories with Gaussian noise added. A brief description of each category is as follows: **AirTemperature** consists of hourly air temperature between 03/01 and 03/31 from 2009 to 2019, collected from CIMIS station 44 in Riverside, CA. **PowerDemand** consists of Italian power demand data between 1/1/1995 and 5/31/1998. **InternalBleeding** consists of the arterial blood pressure measurements of pigs. **EPG** is collected from an insect known as Asian Citrus Psyllid, recorded using an Electropalatography (EPG) apparatus. **NASA T-1** is collected from NASA Mars Science Laboratory (MSL) dataset that consists of spacecraft telemetry signals. Detailed statistics of each category and all the datasets is presented in Table 2.

Operation	Kernel	Strides	Units	BN?	Activation
Encoder					
Convolution	7×7	3×3	48	✓	ReLU
Convolution	5×5	3×3	96	✓	ReLU
Convolution	4×4	2×2	192	✓	ReLU
Convolution	2×2	1×1	z_dim	×	–
Decoder					
Transp. Conv	2×2	1×1	192	✓	LReLU
Transp. Conv	4×4	2×2	96	✓	LReLU
Transp. Conv	5×5	3×3	48	✓	LReLU
Transp. Conv	7×7	3×3	2	×	Tanh
Critic X					
Convolution	7×7	3×3	48	LN	LReLU
Convolution	5×5	3×3	96	LN	LReLU
Convolution	4×4	2×2	192	LN	LReLU
Convolution	2×2	1×1	1	×	–
Critic Z					
Fully Conn.			50	LN	ReLU
Fully Conn.			25	LN	ReLU
Fully Conn.			1	×	–
Hyperparams.					
z_dim	100	Lrn. rate (α)	1e-4	Iterations	5000
Optimizer	RMSProp	Wt decay (λ_{wd})	1e-4	BatchSize	128

Table 1: Architecture of our proposed TSI-GAN. Transp. Conv: Transposed Convolution; BN: Batch Normalization; LN: Layer Normalization respectively; LReLU: LeakyReLU; Lrn. rate: learning rate.

³ UCR 2021 anomaly detection dataset: <https://bit.ly/3V2n6FY>

Model	AirTemperature		PowerDemand		InternalBleeding		EPG		NASA T-1		Noise	All 250 datasets	
	Orig.	Distor.	Orig.	Distor.	Orig.	Distor.	Orig.	Distor.	Orig.	Distor.		F1	Precision
TSI-GAN	1.0	0.833	0.667	0.667	0.846	0.474	0.5	0.556	0.933	0.267	0.479	0.468	0.445
MERLIN	0.054	0.18	0.04	0.071	0.926	0.721	0.354	0.191	0.613	0.6	0.49	0.414	0.402
LSTM-AE	0.389	0.611	0.375	0.583	0.654	0.308	0.222	0.444	0.533	0.333	0.208	0.355	0.301
DONUT	0.611	0.444	0.083	0.1	0.59	0.564	0.278	0.167	0.333	0.533	0.458	0.351	0.325
LSTM-DT	0.778	0.833	0.25	0.5	0.615	0.449	0.222	0.222	0.6	0.6	0.271	0.32	0.289
DENSE-AE	0.194	0.111	0.0	0.0	0.231	0.077	0.222	0.222	0.2	0.0	0.271	0.159	0.136
TadGAN	0.0	0.133	0.0	0.0	0.282	0.24	0.233	0.189	0.267	0.2	0.171	0.131	0.092
Azure	0.181	0.199	0.083	0.196	0.099	0.176	0.167	0.167	0.007	0.017	0.084	0.05	0.037
Luminol	0.022	0.021	0.078	0.089	0.118	0.046	0.037	0.088	0.009	0.014	0.019	0.049	0.021

Table 3: Average F1-Score on original and distorted datasets for each category, as well as F1-Score and Precision averaged over all the 250 datasets.

5.2 Performance Metrics

In real-world application scenarios, most anomalies happen in the form of collective anomalies and hence we use the window-based rules introduced by Hundman et al. [8]: (1) If an anomalous window overlaps any predicted window, a true positive (TP) is recorded; (2) If a predicted window does not overlap with any anomalous window, a false positive (FP) is recorded; (3) If an anomalous window does not overlap with any predicted window, a false negative (FN) is recorded. Based on this set of rules, we calculate *Precision* and *F1-Score* as the performance metrics.

5.3 Experimental Results

Table 3 reports the average F1-Score on the original and distorted datasets for each category, and in the last column, the F1-Score and Precision averaged over all the 250 datasets.

Overall, it is observed that TSI-GAN achieves an F1-Score of 0.468 and Precision of 0.445, outperforming all the baseline methods. More specifically, TSI-GAN offers an improvement of 13% and 31% on F1-score over the second and the third best methods, MERLIN (0.414) and LSTM-AE (0.355), respectively. We note that 85-95% of the improvement was attributed to GAN, while 5-15% was attributed to post-processing. When the individual categories are considered, TSI-GAN performs the best on AirTemperature, PowerDemand, EPG for both original and distorted datasets and wins over other methods by a significant margin; it also offers competitive performance on other categories (InternalBleeding, NASA-T1 Distorted, and Noise) as well.

Using MERLIN as a benchmark, we measure the performance difference between each method and MERLIN in Fig. 3. It indicates that TSI-GAN is the only one that offers a positive performance improvement while all the other methods underperform MERLIN.

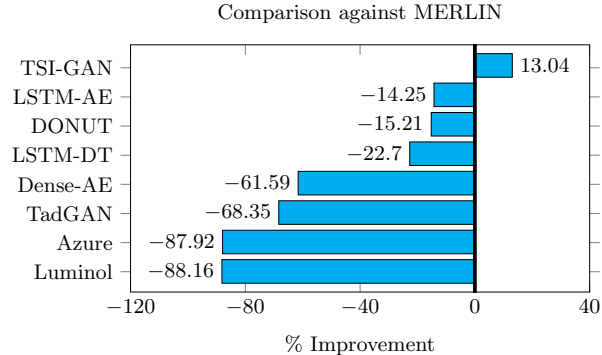


Fig. 3: Comparing all anomaly detection methods against MERLIN in terms of F1 score averaged across all 250 datasets, expressed as a percentage of improvement.

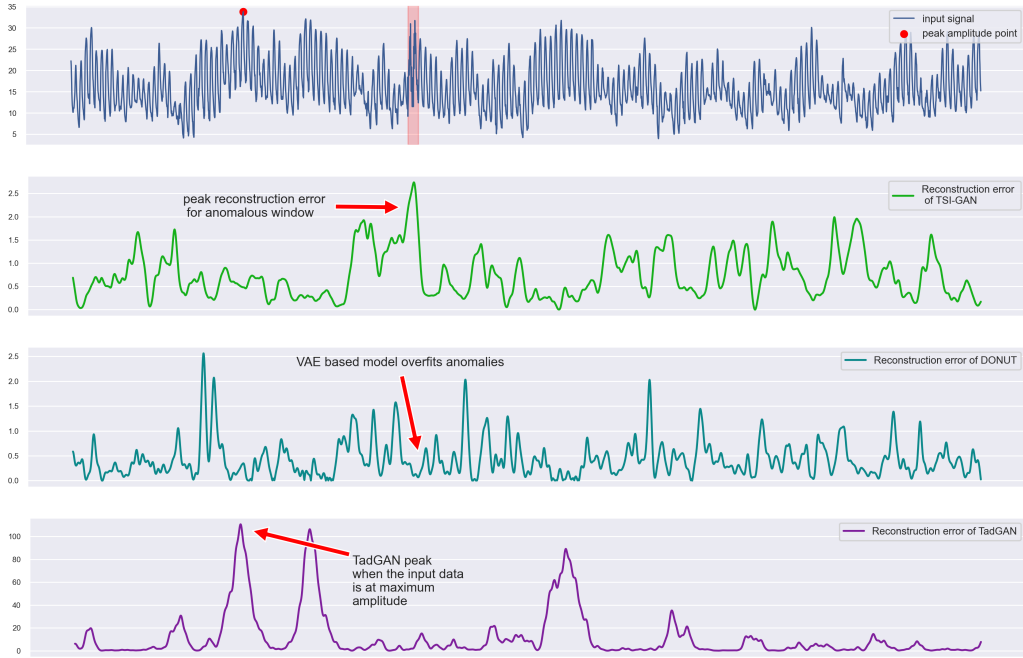


Fig. 4: Illustration of TSI-GAN vs. DONUT vs. TadGAN when applied to an example time series. The translucent red interval depicts the ground-truth anomaly.

Among all the deep learning-based methods, LSTM-AE performs the best, with an average F1-Score of 0.355; DONUT comes in second with a slightly lower score of 0.351. We examine the possible reasons for their shortfall as compared to TSI-GAN and how our approach overcomes them. As we mentioned earlier, autoencoder-based methods carry the risk of overfitting anomalies during training, by reconstructing anomalous samples just as accurately as normal samples. DONUT which employs VAE has this tendency as can be seen in Fig. 4. This is also a plausible reason for the underperformance of other autoencoder-based models such as LSTM-AE.

In contrast, TSI-GAN uses an adversarial training strategy which makes our model largely immune to this behavior. However, while TadGAN and many others alike also use adversarial learning, they are unable to capture anomalies that are not amplitude spikes or dips unless dataset-specific parameters such as sampling interval are known. The reason is that they do not instrument feature engineering to capture anomalies that deviate in seasonality, trend, etc., and therefore tend to only detect extremely high or low amplitude points in the input as can be observed in Fig. 4. It is the main reason why TadGAN only performs well on datasets in which all anomalies are either amplitude spikes or dips; such anomalies, however, are *trivial* to detect as pointed out by [21]. On the other hand, TSI-GAN uses GAF and RP encoding which substantially enhances its ability to detect various types of non-trivial deviance, as can be observed in Fig. 4.

Time Efficiency. We report the training and inference time of TSI-GAN in Table 4. The times are measured on a NVIDIA RTX 3070 GPU with 8GB of VRAM along with AMD Ryzen 7 5800H @ 3.20 GHz CPU.

	AirTemperature			PowerDemand		
	# of Samples	Total time	Per-window time	# of Samples	Total time	Per-window time
Training	7996	251s	0.06s	29772	246s	0.01s
Inference	4083	10s	0.002s	11862	27s	0.002s

Table 4: Training and Inference time of TSI-GAN

We can see that the training time remains almost constant irrespective of the number of training samples, the reason is that we train for iterations and not epochs. More importantly, the inference time per window is only two milliseconds, which signifies that TSI-GAN is well suited for use on rapidly arriving streaming data.

6 Conclusion

In this paper, we introduce TSI-GAN, a novel convolutional cycle-consistent GAN architecture that learns to reconstruct 2D-encoded time-series data and produces effective and reliable reconstruction errors for detecting time series anomalies. We also address the challenge of mitigating false alarms by post-processing the reconstruction error using a filtering technique and computing a reliable score by combining two channels. Our extensive experimental results demonstrate that TSI-GAN outperforms 8 state-of-the-art baseline methods over 250 non-trivial datasets that are well-curated. We also provide an in-depth analysis of the baselines’ limitations and how our model addresses them. TSI-GAN is unsupervised and generalizes well without the need for parameter calibration, enabling it to be applicable to many applications that involve time series.

References

1. Angiulli, F., Pizzuti, C.: Fast outlier detection in high dimensional spaces. In: European conference on principles of data mining and knowledge discovery. pp. 15–27. Springer (2002)
2. Çelik, M., Dadaşer-Çelik, F., Dokuz, A.Ş.: Anomaly detection in temperature data using dbSCAN algorithm. In: 2011 international symposium on innovations in intelligent systems and applications. pp. 91–95. IEEE (2011)
3. Chawla, S., Gionis, A.: k-means-: A unified approach to clustering and outlier detection. In: Proceedings of the 2013 SIAM international conference on data mining. pp. 189–197. SIAM (2013)
4. Eckmann, J.P., Kamphorst, S.O., Ruelle, D., et al.: Recurrence plots of dynamical systems. World Scientific Series on Nonlinear Science Series A **16**, 441–446 (1995)
5. Geiger, A., Liu, D., Alnegheimish, S., Cuesta-Infante, A., Veeramachaneni, K.: Tadgan: Time series anomaly detection using generative adversarial networks. In: 2020 IEEE International Conference on Big Data (Big Data). pp. 33–43. IEEE (2020)
6. Gulrajani, I., Ahmed, F., Arjovsky, M., Dumoulin, V., Courville, A.C.: Improved training of wasserstein GANs. In: Guyon, I., Luxburg, U.V., Bengio, S., Wallach, H., Fergus, R., Vishwanathan, S., Garnett, R. (eds.) Advances in Neural Information Processing Systems. vol. 30. Curran Associates, Inc. (2017)
7. Hodrick, R.J., Prescott, E.C.: Postwar us business cycles: an empirical investigation. Journal of Money, credit, and Banking pp. 1–16 (1997)
8. Hundman, K., Constantinou, V., Laporte, C., Colwell, I., Soderstrom, T.: Detecting spacecraft anomalies using lSTMs and nonparametric dynamic thresholding. In: Proceedings of the 24th ACM SIGKDD international conference on knowledge discovery & data mining. pp. 387–395 (2018)
9. Isola, P., Zhu, J.Y., Zhou, T., Efros, A.A.: Image-to-image translation with conditional adversarial networks. In: Proceedings of the IEEE conference on computer vision and pattern recognition. pp. 1125–1134 (2017)

10. Levina, E., Bickel, P.: The earth mover's distance is the mallows distance: Some insights from statistics. In: Proceedings Eighth IEEE International Conference on Computer Vision (ICCV). vol. 2, pp. 251–256. IEEE (2001)
11. Li, D., Chen, D., Jin, B., Shi, L., Goh, J., Ng, S.K.: Mad-gan: Multivariate anomaly detection for time series data with generative adversarial networks. In: International conference on artificial neural networks. pp. 703–716. Springer (2019)
12. LinkedIn: Luminol (2015), <https://github.com/linkedin/luminol>, access 15 May 2022
13. Nakamura, T., Imamura, M., Mercer, R., Keogh, E.: Merlin: Parameter-free discovery of arbitrary length anomalies in massive time series archives. In: 2020 IEEE International Conference on Data Mining (ICDM). pp. 1190–1195. IEEE (2020)
14. Nguyen, H., Tran, K.P., Thomassey, S., Hamad, M.: Forecasting and anomaly detection approaches using lstm and lstm autoencoder techniques with the applications in supply chain management. *International Journal of Information Management* **57**, 102282 (2021)
15. Pena, E.H., de Assis, M.V., Proença, M.L.: Anomaly detection using forecasting methods arima and hws. In: 2013 32nd international conference of the chilean computer science society (sccc). pp. 63–66. IEEE (2013)
16. Ren, H., Xu, B., Wang, Y., Yi, C., Huang, C., Kou, X., Xing, T., Yang, M., Tong, J., Zhang, Q.: Time-series anomaly detection service at microsoft. In: Proceedings of the 25th ACM SIGKDD international conference on knowledge discovery & data mining. pp. 3009–3017 (2019)
17. Sakurada, M., Yairi, T.: Anomaly detection using autoencoders with nonlinear dimensionality reduction. In: Proceedings of the MLSDA 2014 2nd workshop on machine learning for sensory data analysis. pp. 4–11 (2014)
18. Schlegl, T., Seeböck, P., Waldstein, S.M., Schmidt-Erfurth, U., Langs, G.: Unsupervised anomaly detection with generative adversarial networks to guide marker discovery. In: International conference on information processing in medical imaging. pp. 146–157. Springer (2017)
19. Wang, Z., Oates, T.: Encoding time series as images for visual inspection and classification using tiled convolutional neural networks. In: Workshops at the twenty-ninth AAAI conference on artificial intelligence (2015)
20. Wei, L., Kumar, N., Lolla, V.N., Keogh, E.J., Lonardi, S., Ratanamahatana, C.A.: Assumption-free anomaly detection in time series. In: SSDBM. vol. 5, pp. 237–242 (2005)
21. Wu, R., Keogh, E.: Current time series anomaly detection benchmarks are flawed and are creating the illusion of progress. *IEEE Transactions on Knowledge and Data Engineering* (2021)
22. Xu, H., Chen, W., Zhao, N., Li, Z., Bu, J., Li, Z., Liu, Y., Zhao, Y., Pei, D., Feng, Y., et al.: Unsupervised anomaly detection via variational auto-encoder for seasonal kpis in web applications. In: Proceedings of the 2018 World Wide Web Conference on World Wide Web. pp. 187–196. International World Wide Web Conferences Steering Committee (2018)
23. Xu, L., Zheng, L., Li, W., Chen, Z., Song, W., Deng, Y., Chang, Y., Xiao, J., Yuan, B.: Nvae-gan based approach for unsupervised time series anomaly detection. arXiv preprint arXiv:2101.02908 (2021), not peer-reviewed or published, code not available
24. Yankov, D., Keogh, E., Rebbapragada, U.: Disk aware discord discovery: finding unusual time series in terabyte sized datasets. *Knowledge and Information Systems* **17**(2), 241–262 (2008)
25. Zenati, H., Romain, M., Foo, C.S., Lecouat, B., Chandrasekhar, V.: Adversarially learned anomaly detection. In: 2018 IEEE International conference on data mining (ICDM). pp. 727–736. IEEE (2018)
26. Zhu, J.Y., Park, T., Isola, P., Efros, A.A.: Unpaired image-to-image translation using cycle-consistent adversarial networks. In: Proceedings of the IEEE international conference on computer vision. pp. 2223–2232 (2017)